Optical Properties and Raman Spectroscopy of Carbon Nanotubes

Riichiro Saito[1] and Hiromichi Kataura[2]

[1] Department of Electronic-Engineering, The University of Electro-Communications
1-5-1, Chofu-gaoka, Chofu, Tokyo 182-8585, Japan
rsaito@tube.ee.uec.ac.jp
[2] Department of Physics, Tokyo Metropolitan University
1-1 Minami-Ohsawa, Hachioji, Tokyo 192-0397, Japan
kataura@phys.metro-u.ac.jp

Abstract. The optical properties and the resonance Raman spectroscopy of single wall carbon nanotubes are reviewed. Because of the unique van Hove singularities in the electronic density of states, resonant Raman spectroscopy has provided diameter-selective observation of carbon nanotubes from a sample containing nanotubes with different diameters. The electronic and phonon structure of single wall carbon nanotubes are reviewed, based on both theoretical considerations and spectroscopic measurements.

The quantum properties of Single-Wall Carbon Nanotubes (SWNTs) depend on the diameter and chirality, which is defined by the indices (n, m) [1,2]. Chirality is a term used to specify a nanotube structure, which does not have mirror symmetry. The synthesis of a SWNT sample with a single chirality is an ultimate objective for carbon nanotube physics and material science research, but this is still difficult to achieve with present synthesis techniques. On the other hand, the diameter of SWNTs can now be controlled significantly by changing the furnace growth temperature and catalysts [3,4,5,6]. Thus, a mixture of SWNTs with different chiralities, but with a small range of nanotube diameters is the best sample that can be presently obtained. Resonance Raman spectroscopy provides a powerful tool to investigate the geometry of SWNTs for such samples and we show here that metallic and semiconducting carbon nanotubes can be separately observed in the resonant Raman signal.

In this paper, we first review theoretical issues concerning the electron and phonon properties of a single-walled carbon nanotube. We then describe the electronic and phonon density of states of SWNTs. In order to discuss resonant Raman experiments, we make a plot of the possible energies of optical transitions as a function of the diameter of SWNTs.

Then we review experimental issues concerning the diameter-controlled synthesis of SWNTs and Raman spectroscopy by many laser frequencies. The optical absorption measurements of SWNTs are in good agreement with the theoretical results.

M. S. Dresselhaus, G. Dresselhaus, Ph. Avouris (Eds.): Carbon Nanotubes,
Topics Appl. Phys. **80**, 213–247 (2001)

1 Theoretical Issues

The electronic structure of carbon nanotubes is unique in solid-state physics in the sense that carbon nanotubes can be either semiconducting or metallic, depending on their diameter and chirality [1,2]. The phonon properties are also remarkable, showing unique one-dimensional (1D) behavior and special characteristics related to the cylindrical lattice geometry, such as the Radial Breathing Mode (RBM) properties and the special twist acoustic mode which is unique among 1D phonon subbands.

Using the simple tight-binding method and pair-wise atomic force constant models, we can derive the electronic and phonon structure, respectively. These models provide good approximations for understanding the experimental results for SWNTs.

1.1 Electronic Structure and Density of States of SWNTs

We now introduce the basic definitions of the carbon nanotube structure and of the calculated electronic and phonon energy bands with their special Density of States (DOS). The structure of a SWNT is specified by the chiral vector $\mathbf{C}_h$

$$\mathbf{C}_h = n\mathbf{a}_1 + m\mathbf{a}_2 \equiv (n, m)\,, \tag{1}$$

where $\mathbf{a}_1$ and $\mathbf{a}_2$ are unit vectors of the hexagonal lattice shown in Fig. 1. The vector $\mathbf{C}_h$ connects two crystallographically equivalent sites O and A on a two-dimensional (2D) graphene sheet, where a carbon atom is located at each vertex of the honeycomb structure [7]. When we join the line AB' to the parallel line OB in Fig. 1, we get a seamlessly joined SWNT classified by the integers (n, m), since the parallel lines AB' and OB cross the honeycomb lattice at equivalent points. There are only two kinds of SWNTs which have mirror symmetry: zigzag nanotubes $(n, 0)$, and armchair nanotubes (n, n). The other nanotubes are called chiral nanotubes, and they have axial chiral symmetry. The general chiral nanotube has chemical bonds that are not

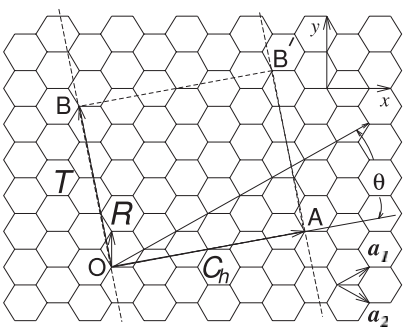

Fig. 1. The unrolled honeycomb lattice of a nanotube. When we connect sites O and A, and sites B and B', a nanotube can be constructed. $\overrightarrow{OA}$ and $\overrightarrow{OB}$ define the chiral vector $\mathbf{C}_h$ and the translational vector $\mathbf{T}$ of the nanotube, respectively. The rectangle $OAB'B$ defines the unit cell for the nanotube. The figure is constructed for an $(n, m) = (4, 2)$ nanotube [2]

parallel to the nanotube axis, denoted by the chiral angle θ in Fig. 1. Here the direction of the nanotube axis corresponds to OB in Fig. 1. The zigzag, armchair and chiral nanotubes correspond, respectively, to $\theta = 0°$, $\theta = 30°$, and $0 \le |\theta| \le 30°$. In a zigzag or an armchair nanotube, respectively, one of three chemical bonds from a carbon atom is parallel or perpendicular to the nanotube axis.

The diameter of a (n, m) nanotube d_t is given by

$$d_t = C_h/\pi = \sqrt{3}a_{C-C}(m^2 + mn + n^2)^{1/2}/\pi \tag{2}$$

where a_{C-C} is the nearest-neighbor C–C distance (1.42 Å in graphite), and C_h is the length of the chiral vector $\mathbf{C}_h$. The chiral angle θ is given by

$$\theta = \tan^{-1}[\sqrt{3}m/(m + 2n)]. \tag{3}$$

The 1D electronic DOS is given by the energy dispersion of carbon nanotubes which is obtained by zone folding of the 2D energy dispersion relations of graphite. Hereafter we only consider the valence π and the conduction π^* energy bands of graphite and nanotubes. The 2D energy dispersion relations of graphite are calculated [2] by solving the eigenvalue problem for a (2×2) Hamiltonian $\mathcal{H}$ and a (2×2) overlap integral matrix $\mathcal{S}$, associated with the two inequivalent carbon atoms in 2D graphite,

$$\mathcal{H} = \begin{pmatrix} \epsilon_{2p} & -\gamma_0 f(k) \\ -\gamma_0 f(k)^* & \epsilon_{2p} \end{pmatrix} \text{ and } \mathcal{S} = \begin{pmatrix} 1 & sf(k) \\ sf(k)^* & 1 \end{pmatrix} \tag{4}$$

where ϵ_{2p} is the site energy of the $2p$ atomic orbital and

$$f(k) = \mathrm{e}^{\mathrm{i}k_x a/\sqrt{3}} + 2\mathrm{e}^{-\mathrm{i}k_x a/2\sqrt{3}} \cos\frac{k_y a}{2} \tag{5}$$

where $a = |\mathbf{a}_1| = |\mathbf{a}_2| = \sqrt{3}a_{C-C}$. Solution of the secular equation $\det(\mathcal{H} - E\mathcal{S}) = 0$ implied by (4) leads to the eigenvalues

$$E^{\pm}_{g2D}(\boldsymbol{k}) = \frac{\epsilon_{2p} \pm \gamma_0 w(\boldsymbol{k})}{1 \mp s w(\boldsymbol{k})} \tag{6}$$

for the C-C transfer energy $\gamma_0 > 0$, where s denotes the overlap of the electronic wave function on adjacent sites, and E^+ and E^- correspond to the π^* and the π energy bands, respectively. Here we conventionally use γ_0 as a positive value. The function $w(\boldsymbol{k})$ in (6) is given by

$$w(\boldsymbol{k}) = \sqrt{|f(\boldsymbol{k})|^2} = \sqrt{1 + 4\cos\frac{\sqrt{3}k_x a}{2}\cos\frac{k_y a}{2} + 4\cos^2\frac{k_y a}{2}}. \tag{7}$$

In Fig. 2 we plot the electronic energy dispersion relations for 2D graphite as a function of the two-dimensional wave vector $\boldsymbol{k}$ in the hexagonal Brillouin zone in which we adopt the parameters $\gamma_0 = 3.013\,\mathrm{eV}$, $s = 0.129$ and $\epsilon_{2p} = 0$

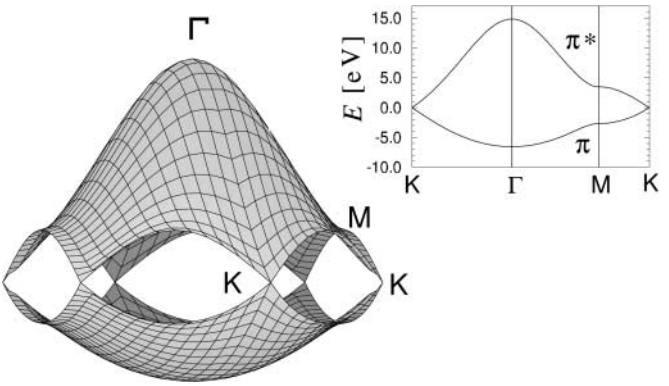

Fig. 2. The energy dispersion relations for 2D graphite with $\gamma_0 = 3.013\,\mathrm{eV}$, $s = 0.129$ and $\epsilon_{2p} = 0$ in (6) are shown throughout the whole region of the Brillouin zone. The inset shows the energy dispersion along the high symmetry lines between the Γ, M, and K points. The valence π band (*lower part*) and the conduction π^* band (*upper part*) are degenerate at the K points in the hexagonal Brillouin zone which corresponds to the Fermi energy [2]

so as to fit both the first principles calculation of the energy bands of 2D turbostratic graphite [8,9] and experimental data [2,10]. The corresponding energy contour plot of the 2D energy bands of graphite with $s = 0$ and $\epsilon_{2p} = 0$ is shown in Fig. 3. The Fermi energy corresponds to $E = 0$ at the K points.

Near the K-point at the corner of the hexagonal Brillouin zone of graphite, $w(\boldsymbol{k})$ has a linear dependence on $k \equiv |\boldsymbol{k}|$ measured from the K point as

$$w(\boldsymbol{k}) = \frac{\sqrt{3}}{2}ka + \ldots, \qquad \text{for } \; ka \ll 1. \tag{8}$$

Thus, the expansion of (6) for small k yields

$$E^{\pm}_{g2\mathrm{D}}(\boldsymbol{k}) = \epsilon_{2p} \pm (\gamma_0 - s\epsilon_{2p})w(\boldsymbol{k}) + \ldots\,, \tag{9}$$

so that in this approximation, the valence and conduction bands are symmetric near the K point, independent of the value of s. When we adopt $\epsilon_{2p} = 0$ and take $s = 0$ for (6), and assume a linear k approximation for $w(k)$, we get the linear dispersion relations for graphite given by [12,13]

$$E(k) = \pm\frac{\sqrt{3}}{2}\gamma_0 ka = \pm\frac{3}{2}\gamma_0 k a_{\mathrm{C-C}}\,. \tag{10}$$

If the physical phenomena under consideration only involve small k vectors, it is convenient to use (10) for interpreting experimental results relevant to such phenomena.

The 1D energy dispersion relations of a SWNT are given by

$$\begin{aligned} E^{\pm}_{\mu}(k) = E^{\pm}_{g2\mathrm{D}}\left(k\frac{\mathbf{K}_2}{|\mathbf{K}_2|} + \mu\mathbf{K}_1\right), \\ \left(-\frac{\pi}{T} < k < \frac{\pi}{T}, \text{ and } \mu = 1, \cdots, N\right), \end{aligned} \tag{11}$$

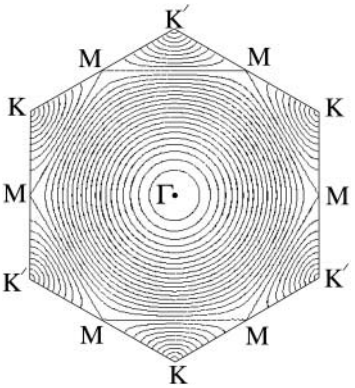

Fig. 3. Contour plot of the 2D electronic energy of graphite with $s = 0$ and $\epsilon_{2p} = 0$ in (6). The equi-energy lines are circles near the K point and near the center of the hexagonal Brillouin zone, but are straight lines which connect nearest M points. Adjacent lines correspond to changes in height (energy) of $0.1\gamma_0$ and the energy value for the K, M and Γ points are 0, γ_0 and $3\gamma_0$, respectively. It is useful to note the coordinates of high symmetry points: $K = (0, 4\pi/3a)$, $M = (2\pi/\sqrt{3}a, 0)$ and $\Gamma = (0, 0)$, where a is the lattice constant of the 2D sheet of graphite [11]

where T is the magnitude of the translational vector $\mathbf{T}$, k is a 1D wave vector along the nanotube axis, and N denotes the number of hexagons of the graphite honeycomb lattice that lie within the nanotube unit cell (see Fig. 1). T and N are given, respectively, by

$$T = \frac{\sqrt{3}C_h}{d_\mathrm{R}} = \frac{\sqrt{3}\pi d_\mathrm{t}}{d_\mathrm{R}}, \quad \text{and} \quad N = \frac{2(n^2 + m^2 + nm)}{d_\mathrm{R}}. \tag{12}$$

Here d_R is the greatest common divisor of $(2n + m)$ and $(2m + n)$ for a (n, m) nanotube [2,14]. Further $\mathbf{K}_1$ and $\mathbf{K}_2$ denote, respectively, a discrete unit wave vector along the circumferential direction, and a reciprocal lattice vector along the nanotube axis direction, which for a (n, m) nanotube are given by

$$\begin{aligned} \mathbf{K}_1 &= \{(2n + m)\mathbf{b}_1 + (2m + n)\mathbf{b}_2\}/Nd_\mathrm{R} \qquad \text{and} \\ \mathbf{K}_2 &= (m\mathbf{b}_1 - n\mathbf{b}_2)/N, \end{aligned} \tag{13}$$

where $\mathbf{b}_1$ and $\mathbf{b}_2$ are the reciprocal lattice vectors of 2D graphite and are given in x, y coordinates by

$$\mathbf{b}_1 = \left(\frac{1}{\sqrt{3}}, 1\right)\frac{2\pi}{a}, \qquad \mathbf{b}_2 = \left(\frac{1}{\sqrt{3}}, -1\right)\frac{2\pi}{a}. \tag{14}$$

The periodic boundary condition for a carbon nanotube (n, m) gives N discrete k values in the circumferential direction. The N pairs of energy dispersion curves given by (11) correspond to the cross sections of the two-dimensional energy dispersion surface shown in Fig. 2, where cuts are made on

the lines of $k\mathbf{K}_2/|\mathbf{K}_2| + \mu\mathbf{K}_1$. In Fig. 4 several cutting lines near one of the K points are shown. The separation between two adjacent lines and the length of the cutting lines are given by the $\mathbf{K}_1$ and $\mathbf{K}_2$ vectors of (13), respectively, whose lengths are given by

$$|\mathbf{K}_1| = \frac{2}{d_\mathrm{t}}, \quad \text{and} \quad |\mathbf{K}_2| = \frac{2\pi}{T} = \frac{2d_\mathrm{R}}{\sqrt{3}d_\mathrm{t}}. \tag{15}$$

If, for a particular (n, m) nanotube, the cutting line passes through a K point of the 2D Brillouin zone (Fig. 4a), where the π and π^* energy bands of 2D graphite are degenerate (Fig. 2) by symmetry, then the 1D energy bands have a zero energy gap. Since the degenerate point corresponds to the Fermi energy, and the density of states are finite as shown below, SWNTs with a zero band gap are metallic. When the K point is located between two cutting lines, the K point is always located in a position one-third of the distance between two adjacent $\mathbf{K}_1$ lines (Fig. 4b) [14] and thus a semiconducting nanotube with a finite energy gap appears. The rule for being either a metallic or a semiconducting carbon nanotube is, respectively, that $n - m = 3q$ or $n - m \neq 3q$, where q is an integer [2,8,15,16,17].

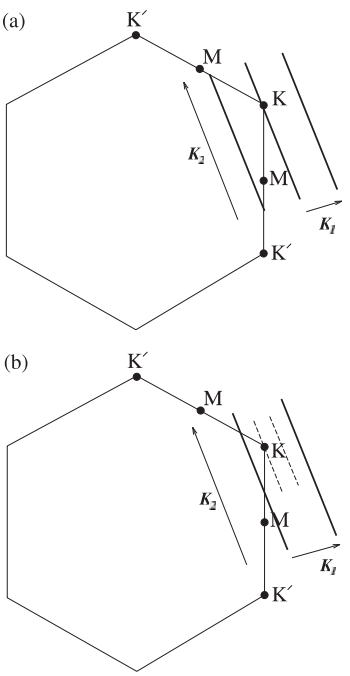

Fig. 4. The wave vector k for one-dimensional carbon nanotubes is shown in the two-dimensional Brillouin zone of graphite (hexagon) as bold lines for (**a**) metallic and (**b**) semiconducting carbon nanotubes. In the direction of $\mathbf{K}_1$, discrete k values are obtained by periodic boundary conditions for the circumferential direction of the carbon nanotubes, while in the direction of the $\mathbf{K}_2$ vector, continuous k vectors are shown in the one-dimensional Brillouin zone. (**a**) For metallic nanotubes, the bold line intersects a K point (corner of the hexagon) at the Fermi energy of graphite. (**b**) For the semiconductor nanotubes, the K point always appears one-third of the distance between two bold lines. It is noted that only a few of the N bold lines are shown near the indicated K point. For each bold line, there is an energy minimum (or maximum) in the valence and conduction energy subbands, giving rise to the energy differences $E_{pp}(d_\mathrm{t})$

The 1D density of states (DOS) in units of states/C-atom/eV is calculated by

$$D(E) = \frac{T}{2\pi N} \sum_{\pm} \sum_{\mu=1}^{N} \int \frac{1}{\left| \frac{dE_{\mu}^{\pm}(k)}{dk} \right|} \delta(E_{\mu}^{\pm}(k) - E) dE, \tag{16}$$

where the summation is taken for the N conduction $(+)$ and valence $(-)$ 1D bands. Since the energy dispersion near the Fermi energy (10) is linear, the density of states of metallic nanotubes is constant at the Fermi energy: $D(E_{\mathrm{F}}) = a/(2\pi^2 \gamma_0 d_{\mathrm{t}})$, and is inversely proportional to the diameter of the nanotube. It is noted that we always have two cutting lines (1D energy bands) at the two equivalent symmetry points K and K' in the 2D Brillouin zone in Fig. 3. The integrated value of $D(E)$ for the energy region of $E_{\mu}(k)$ is 2 for any (n, m) nanotube, which includes the plus and minus signs of $E_{g2\mathrm{D}}$ and the spin degeneracy.

It is clear from (16) that the density of states becomes large when the energy dispersion relation becomes flat as a function of k. One-dimensional van Hove singularities (vHs) in the DOS, which are known to be proportional to $(E^2 - E_0^2)^{-1/2}$ at both the energy minima and maxima $(\pm E_0)$ of the dispersion relations for carbon nanotubes, are important for determining many solid state properties of carbon nanotubes, such as the spectra observed by scanning tunneling spectroscopy (STS), [18,19,20,21,22], optical absorption [4,23,24], and resonant Raman spectroscopy [25,26,27,28,29].

The one-dimensional vHs of SWNTs near the Fermi energy come from the energy dispersion along the bold lines in Fig. 4 near the K point of the Brillouin zone of 2D graphite. Within the linear k approximation for the energy dispersion relations of graphite given by (10), the energy contour as shown in Fig. 3 around the K point is circular and thus the energy minima of the 1D energy dispersion relations are located at the closest positions to the K point. Using the small k approximation of (10), the energy differences $E_{11}^{\mathrm{M}}(d_{\mathrm{t}})$ and $E_{11}^{\mathrm{S}}(d_{\mathrm{t}})$ for metallic and semiconducting nanotubes between the highest-lying valence band singularity and the lowest-lying conduction band singularity in the 1D electronic density of states curves are expressed by substituting for k the values of $|\mathbf{K}_1|$ of (15) for metallic nanotubes and of $|\mathbf{K}_1/3|$ and $|2\mathbf{K}_1/3|$ for semiconducting nanotubes, respectively [30,31], as follows:

$$E_{11}^{\mathrm{M}}(d_{\mathrm{t}}) = 6a_{\mathrm{C-C}}\gamma_0/d_{\mathrm{t}} \quad \text{and} \quad E_{11}^{\mathrm{S}}(d_{\mathrm{t}}) = 2a_{\mathrm{C-C}}\gamma_0/d_{\mathrm{t}}. \tag{17}$$

When we use the number p $(p = 1, 2, \ldots)$ to denote the order of the valence π and conduction π^* energy bands symmetrically located with respect to the Fermi energy, optical transitions $E_{pp'}$ from the p-th valence band to the p'-th conduction band occur in accordance with the selection rules of $\delta p = 0$ and $\delta p = \pm 1$ for parallel and perpendicular polarizations of the electric field with respect to the nanotube axis, respectively [23]. However, in the case of perpendicular polarization, the optical transition is suppressed

by the depolarization effect [23], and thus hereafter we only consider the optical absorption of $\delta p = 0$. For mixed samples containing both metallic and semiconducting carbon nanotubes with similar diameters, optical transitions may appear with the following energies, starting from the lowest energy, $E_{11}^{\mathrm{S}}(d_{\mathrm{t}})$, $2E_{11}^{\mathrm{S}}(d_{\mathrm{t}})$, $E_{11}^{\mathrm{M}}(d_{\mathrm{t}})$, $4E_{11}^{\mathrm{S}}(d_{\mathrm{t}})$, ...

In Fig. 5, both $E_{pp}^{\mathrm{S}}(d_{\mathrm{t}})$ and $E_{pp}^{\mathrm{M}}(d_{\mathrm{t}})$ are plotted as a function of nanotube diameter d_{t} for all chiral angles at a given d_{t} value. [3,4,11]. This plot is very useful for determining the resonant energy in the resonant Raman spectra corresponding to a particular nanotube diameter. In this figure, we use the values of $\gamma_0 = 2.9eV$ and $s = 0$, which explain the experimental observations discussed in the experimental section.

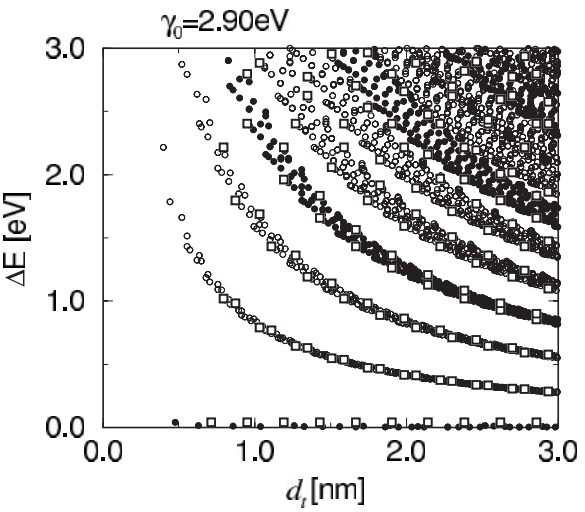

Fig. 5. Calculation of the energy separations $E_{pp}(d_{\mathrm{t}})$ for all (n, m) values as a function of the nanotube diameter between $0.7 < d_{\mathrm{t}} < 3.0\,\mathrm{nm}$ (based on the work of *Kataura* et al. [3]). The results are based on the tight binding model of Eqs. (6) and (7), with $\gamma_0 = 2.9\,\mathrm{eV}$ and $s = 0$. The open and solid circles denote the peaks of semiconducting and metallic nanotubes, respectively. *Squares* denote the $E_{pp}(d_{\mathrm{t}})$ values for zigzag nanotubes which determine the width of each $E_{pp}(d_{\mathrm{t}})$ curve. Note the points for zero gap metallic nanotubes along the abscissa [11]

1.2 Trigonal Warping Effects in the DOS Windows

Within the linear k approximation for the energy dispersion relations of graphite, E_{pp} of (17) depends only on the nanotube diameter, d_{t}. However, the width of the E_{pp} band in Fig. 5 becomes large with increasing E_{pp} [11].

When the value of $|\mathbf{K}_1| = 2/d_{\mathrm{t}}$ is large, which corresponds to smaller values of d_{t}, the linear dispersion approximation is no longer correct. When

we then plot equi-energy lines near the K point (see Fig. 3), we get circular contours for small k values near the K and K' points in the Brillouin zone, but for large k values, the equi-energy contour becomes a triangle which connects the three M points nearest to the K-point (Fig. 6). The distortion in Fig. 3 of the equi-energy lines away from the circular contour in materials with a 3-fold symmetry axis is known as the trigonal warping effect.

In metallic nanotubes, the trigonal warping effects generally split the DOS peaks for metallic nanotubes, which come from the two neighboring lines near the K point (Fig. 6). For armchair nanotubes as shown in Fig. 6a, the two lines are equivalent to each other and the DOS peak energies are equal, while for zigzag nanotubes, as shown in Fig. 6b, the two lines are not equivalent, which gives rise to a splitting of the DOS peak. In a chiral nanotube the two lines are not equivalent in the reciprocal lattice space, and thus the splitting values of the DOS peaks are a function of the chiral angle.

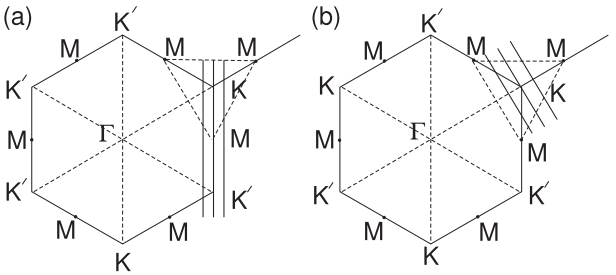

Fig. 6. The trigonal warping effect of the van Hove singularities. The three bold lines near the K point are possible k vectors in the hexagonal Brillouin zone of graphite for metallic (**a**) armchair and (**b**) zigzag carbon nanotubes. The minimum energy along the neighboring two lines gives the energy positions of the van Hove singularities

On the other hand, for semiconducting nanotubes, since the value of the k vectors on the two lines near the K point contribute to different spectra, namely to that of $E_{11}^{\mathrm{S}}(d_{\mathrm{t}})$ and $E_{22}^{\mathrm{S}}(d_{\mathrm{t}})$, there is no splitting of the DOS peaks for semiconducting nanotubes. However, the two lines are not equivalent Fig. 4b, and the $E_{22}^{\mathrm{S}}(d_{\mathrm{t}})$ value is not twice that of $E_{11}^{\mathrm{S}}(d_{\mathrm{t}})$. It is pointed out here that there are two equivalent K points in the hexagonal Brillouin zone denoted by K and K' as shown in Fig. 4, and the values of $E_{ii}^{\mathrm{S}}(d_{\mathrm{t}})$ are the same for the K and K' points. This is because the K and K' points are related to one another by time reversal symmetry (they are at opposite corners from each other in the hexagonal Brillouin zone), and because the chirality of a nanotube is invariant under the time-reversal operation. Thus, the DOS for semiconducting nanotubes will be split if very strong magnetic fields are applied in the direction of the nanotube axis.

The peaks in the 1D electronic density of states of the conduction band measured from the Fermi energy are shown in Fig. 7 for several *metallic* (n, m) nanotubes, all having about the same diameter d_t (from 1.31 nm to 1.43 nm), but having different chiral angles: $\theta = 0°$, 8.9°, 14.7°, 20.2°, 24.8°, and 30.0° for nanotubes (18,0), (15,3), (14,5), (13,7), (11.8), and (10,10), respectively. When we look at the peaks in the 1D DOS as the chiral angle is varied from the armchair nanotube (10,10) ($\theta = 30°$) to the zigzag nanotube (18,0) ($\theta = 0°$) of Fig. 7, the first DOS peaks around $E = 0.9$ eV are split into two peaks whose separation in energy (width) increases with decreasing chiral angle.

This theoretical result [11] is important in the sense that STS (scanning tunneling spectroscopy) [22] and resonant Raman spectroscopy experiments [25,27,28,29] depend on the chirality of an individual SWNT, and therefore trigonal warping effects should provide experimental information about the chiral angle of carbon nanotubes. *Kim* et al. have shown that the DOS of a $(13, 7)$ metallic nanotube has a splitting of the lowest energy peak in their STS spectra [22], and this result provides direct evidence for the trigonal warping effect. Further experimental data will be desirable for a systematic study of this effect. Although the chiral angle is directly observed by scanning tunneling microscopy (STM) [32], corrections to the experimental observations are necessary to account for the effect of the tip size and shape and for the deformation of the nanotube by the tip and by the substrate [33]. We expect that the chirality-dependent DOS spectra are insensitive to such effects.

In Fig. 8 the energy dispersion relations of (6) along the K–Γ and K–M directions are plotted. The energies of the van Hove singularities corresponding

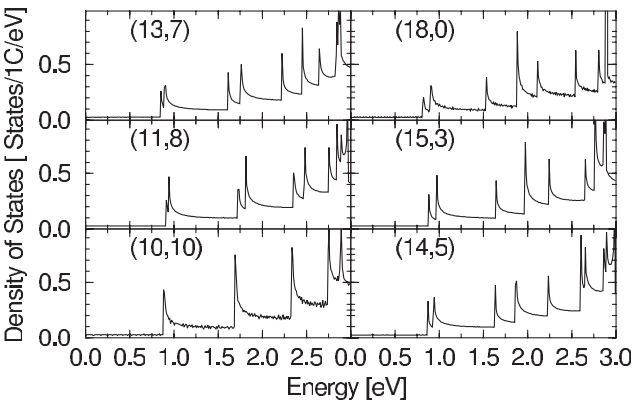

Fig. 7. The 1D electronic density of states vs energy for several metallic nanotubes of approximately the same diameter, showing the effect of chirality on the van Hove singularities: (10,10) (armchair), (11,8), (13,7), (14,5), (15,3) and (18,0) (zigzag). We only show the density of states for the conduction π^* bands

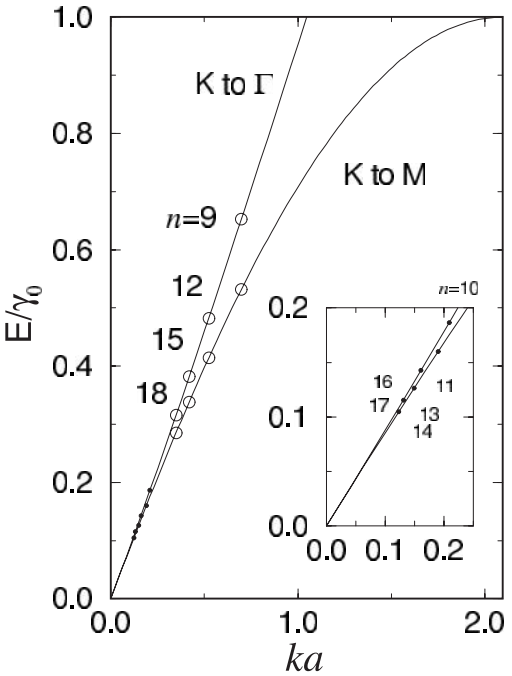

Fig. 8. Splitting of the DOS in zigzag nanotubes. Two minimum energy positions are found in the conduction band for zigzag nanotubes, $(n, 0)$ measured from the energy at the K point. *Open circles* denote metallic carbon nanotubes for $k = |\mathbf{K}_1|$ vectors away from the K point along the $K \to M$ and $K \to \Gamma$ lines, which are the directions of the energy minima (see Fig. 6). (The *inset* shows an expanded view of the figure at small E/γ_0 and small ka for semiconducting nanotubes. The closed circles denote semiconducting carbon nanotubes for $k = |\mathbf{K}_1|/3$ vectors.) Note that the maximum of the horizontal axis corresponds to the M point, $ka = 2\pi/3$, which is measured from the K point. A nanotube diameter of 1 nm corresponds to a (13,0) carbon nanotube

to the lowest 1D energy level are plotted for metallic (open circles) and semiconducting (closed circles) zigzag nanotubes $(n, 0)$ by putting $ka = |\mathbf{K}_1|a$ and $ka = |\mathbf{K}_1|a/3$, respectively. The corresponding energy separation is plotted in Fig. 5 as solid squares. In the case of $(3n + 1, 0)$ and $(3n - 1, 0)$ semiconducting zigzag nanotubes, E_{11}^{S} comes respectively, from the K–Γ and K–M lines, while E_{22}^{S} comes from K–M and K–Γ and so on. In the case of $(3n, 0)$ metallic zigzag nanotubes, the DOS peaks come from both K–M and K–Γ. This systematic rule will be helpful for investigating the STS spectra in detail. Using Eqs. (7) and (15), the widths of E_{11}^{M} and E_{11}^{S}, denoted by $\Delta E_{11}^{\mathrm{M}}$

and $\Delta E_{11}^{\mathrm{S}}$, respectively, are determined by the zigzag nanotubes, and are analytically given by

$$\Delta E_{11}^{\mathrm{M}}(d_{\mathrm{t}}) = 8\gamma_0 \sin^2\left(\frac{a}{2d_{\mathrm{t}}}\right), \quad \Delta E_{11}^{\mathrm{S}}(d_{\mathrm{t}}) = 8\gamma_0 \sin^2\left(\frac{a}{6d_{\mathrm{t}}}\right). \tag{18}$$

Although this trigonal warping effect is proportional to $(a/d_{\mathrm{t}})^2$, the terms in (18) are not negligible, since this correction is the leading term in the expressions for the width $\Delta E_{pp}(d_{\mathrm{t}})$, and the factor 8 before γ_0 makes this correction significant in magnitude for d_{t}=1.4 nm. For example, $E_{11}(d_{\mathrm{t}})$ is split by about 0.18 eV for the metallic $(18, 0)$ zigzag nanotube, and this splitting is large enough to be observable by STS experiments. Although the trigonal warping effect is larger for metallic nanotubes than for semiconducting nanotubes of comparable diameters, the energy difference of the third peaks $E_{33}^{\mathrm{S}}(d_{\mathrm{t}}) = 8\gamma_0 \sin^2(2a/3d_{\mathrm{t}})$ between the $(17, 0)$ and $(19, 0)$ zigzag nanotubes is about 0.63 eV, using an average d_{t} value of 1.43 nm, which becomes easily observable in the experiments. These calculations show that the trigonal warping effect is important for metallic single wall zigzag nanotubes with diameters $d_{\mathrm{t}} < 2$ nm. More direct measurements [22] of the chirality by the STM technique and of the splitting of the DOS by STS measurements on the *same* nanotube would provide very important confirmation of this prediction.

1.3 Phonon Properties

A general approach for obtaining the phonon dispersion relations of carbon nanotubes is given by tight binding molecular dynamics (TBMD) calculations adopted for the nanotube geometry, in which the atomic force potential for general carbon materials is used [25,34]. Here we use the scaled force constants from those of 2D graphite [2,14], and we construct a force constant tensor for a constituent atom of the SWNT so as to satisfy the rotational sum rule for the force constants [35,36]. Since we have $2N$ carbon atoms in the unit cell, the dynamical matrix to be solved becomes a $6N \times 6N$ matrix [35,37].

In Fig. 9 we show the results thus obtained for (a) the phonon dispersion relations $\omega(k)$ and (b) the corresponding phonon density of states for 2D graphite (left) and for a (10,10) armchair nanotube (right). For the $2N = 40$ carbon atoms per circumferential strip for the (10,10) nanotube, we have 120 vibrational degrees of freedom, but because of mode degeneracies, there are only 66 distinct phonon branches, for which 12 modes are non-degenerate and 54 are doubly degenerate. The phonon density of states for the (10,10) nanotube is close to that for 2D graphite, reflecting the zone-folded nanotube phonon dispersion. The same discussion as is used for the electronic structure can be applied to the van Hove singularity peaks in the phonon density of states of carbon nanotubes below a frequency of 400 cm^{-1} which can be observed in neutron scattering experiments for rope samples.

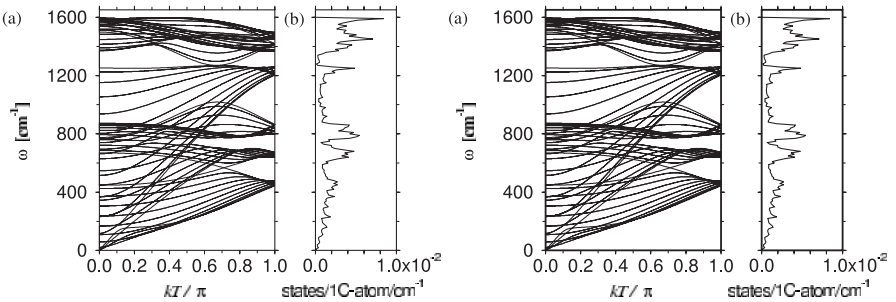

Fig. 9. (**a**) Phonon dispersion relations and (**b**) phonon DOS for 2D graphite (*left*) and for a (10,10) nanotube (*right*) [35]

There are four acoustic modes in a nanotube. The lowest energy acoustic modes are the Transverse Acoustic (TA) modes, which are doubly degenerate, and have x and y displacements perpendicular to the nanotube z axis. The next acoustic mode is the "twisting" acoustic mode (TW), which has θ-dependent displacements along the nanotube surface. The highest energy mode is the Longitudinal Acoustic (LA) mode whose displacements occur in the z direction. The sound velocities of the TA, TW, and LA phonons for a (10,10) carbon nanotube, $v_{\mathrm{TA}}^{(10,10)}$, $v_{\mathrm{TW}}^{(10,10)}$ and $v_{\mathrm{LA}}^{(10,10)}$, are estimated as $v_{\mathrm{TA}}^{(10,10)}$=9.42 km/s, $v_{\mathrm{TW}}^{(10,10)}$ = 15.00 km/s, and $v_{\mathrm{LA}}^{(10,10)}$ =20.35 km/s, respectively. The calculated phase velocity of the in-plane TA and LA modes of 2D graphite are $v_{\mathrm{TA}}^{\mathrm{G}}$=15.00 km/s and $v_{\mathrm{LA}}^{\mathrm{G}}$=21.11 km/s, respectively. Since the TA mode of the nanotube has both an 'in-plane' and an 'out-of-plane' component, the nanotube TA modes are softer than the in-plane TA modes of 2D-graphite. The calculated phase velocity of the out-of-plane TA mode for 2D graphite is almost 0 km/s because of its k^2 dependence. The sound velocities that have been calculated for 2D graphite are similar to those observed in 3D graphite [10], for which $v_{\mathrm{TA}}^{\mathrm{G3D}} = 12.3$ km/s and $v_{\mathrm{LA}}^{\mathrm{G3D}} = 21.0$ km/s. The discrepancy between the v_{TA} velocity of sound for 2D and 3D graphite comes from the interlayer interaction between the adjacent graphene sheets.

The strongest low frequency Raman mode for carbon nanotubes is the Radial Breathing $A_{1\mathrm{g}}$ mode (RBM) whose frequency is calculated to be 165 cm^{-1} for the (10,10) nanotube. Since this frequency is in the silent region for graphite and other carbon materials, this $A_{1\mathrm{g}}$ mode provides a good marker for specifying the carbon nanotube geometry. When we plot the $A_{1\mathrm{g}}$ frequency as a function of nanotube diameter for (n, m) in the range $8 \leq n \leq 10$, $0 \leq m \leq n$, the frequencies are inversely proportional to d_{t} [5,35], within only a small deviation due to nanotube-nanotube interaction in a nanotube bundle. Here $\omega_{(10,10)}$ and $d_{(10,10)}$ are, respectively, the frequency and diameter d_{t} of the (10,10) armchair nanotube, with values of $\omega_{(10,10)}$=165 cm^{-1} and $d_{(10,10)}$=1.357 nm, respectively. However, when we adopt $\gamma_0 = 2.90$ eV, the resonant spectra becomes consistent when we

take $\omega_{(10,10)} = 177\,\mathrm{cm}^{-1}$. As for the higher frequency Raman modes around $1590\,\mathrm{cm}^{-1}$ (G-band), we see some dependence on d_t, since the frequencies of the higher optical modes can be obtained from the zone-folded k values in the phonon dispersion relation of 2D graphite [26].

Using the calculated phonon modes of a SWNT, the Raman intensities of the modes are calculated within the non-resonant bond polarization theory, in which empirical bond polarization parameters are used. [38] The bond parameters that we used in this chapter are $\alpha_\parallel - \alpha_\perp = 0.04$ Å^3, $\alpha'_\parallel + 2\alpha'_\perp = 4.7$ Å^2, and $\alpha'_\parallel - \alpha'_\perp = 4.0$ Å^2, where α and α' denote the polarizability parameters and their derivatives with respect to bond length, respectively. [35] The eigenfunctions for the various vibrational modes are calculated numerically at the Γ point ($k = 0$). When some symmetry-lowering effects, such as defects and finite size effects occur, phonon modes away from the Γ point are observed in the Raman spectra. For example, the DOS peaks at $1620\,\mathrm{cm}^{-1}$ related to the highest energy of the DOS, and some DOS peaks related to M point phonons can be strong. In general, the lower dimensionality causes a broadening in the DOS, but the peak positions do not change much. The $1350\,\mathrm{cm}^{-1}$ peaks (D-band) are known to be defect-related Raman peaks which originate from K point phonons, and exhibit a resonant behavior [39].

2 Experiment Issues

For the experiments described below, SWNTs were prepared by both laser vaporization and electric arc methods. In the laser vaporization method, the second harmonic of the Nd:YAG laser pulse is focused on a metal catalyzed carbon rod located in a quartz tube filled with 500 Torr Ar gas, which is heated to 1200°C in an electric furnace. The laser-vaporized carbon and catalyst are transformed in the furnace to a soot containing SWNTs and nanoparticles containing catalyst species.

2.1 Diameter-Selective Formation of SWNTs

The diameter distribution of the SWNTs can be controlled by changing the temperature of the furnace. In the electric arc method, the dc arc between the catalyzed carbon anode and the pure carbon cathode produces SWNTs in He gas at 500 Torr. In the arc method, the diameters of the SWNTs are controlled by changing the pressure of the He gas. Increasing the temperature makes larger diameter SWNTs, while the higher ambient gas pressure, up to 760 Torr, makes a larger yield and diameter of SWNTs by the carbon arc method.

The diameter of SWNTs can be controlled, too, by adopting different catalysts and different relative concentrations of the catalyst species, such as NiY (4.2 and 1.0 at. %), NiCo (0.6 and 0.6 at. %), Ni (0.6 at. %) and RhPd (1.2 and 1.2 at. %), which have provided the following diameter distributions by the

laser ablation method with a furnace temperature of 1150 to 1200°C, respectively, 1.24–1.58 nm, 1.06–1.45 nm, 1.06–1.45 nm and 0.68–1.00 nm [3,40]. The diameter distribution in each case was determined from TEM experiments and from measurement of the RBM frequencies using Raman spectroscopy and several different laser excitation energies. It is important to note that the determination of the frequency of the RBM does not provide a measurement of the nanotube chirality, though the diameter dependence is well observed by measurement of the RBM frequency. The diameter distribution is then obtained if the RBM of a (10,10) armchair nanotube is taken to be $165\,\mathrm{cm}^{-1}$ RBM and $\gamma_0 = 2.75\,\mathrm{eV}$ [3]. However, if we adopt the value of $\gamma_0 = 2.90\,\mathrm{eV}$, the Raman signal is consistent with $177\,\mathrm{cm}^{-1}$ for a (10,10) armchair nanotube. For these larger values of γ_0 and $\omega_{\mathrm{RBM}}(10,10)$ the diameter distribution for each catalyst given above is shifted upward by 7%. Most of the catalysts, except for the RhPd, show very similar diameter distributions for both the laser vaporization and the electric arc methods at growth conditions giving the highest yield. In the case of the RhPd catalyst, however, no SWNTs are synthesized by the arc discharge method, in contrast to a high yield provided by the laser vaporization method.

2.2 Sample Preparation and Purification

SWNTs are not soluble in any solvent and they cannot be vaporized by heating at least up to 1450°C in vacuum. In order to measure the optical absorption of SWNTs, the sample can be prepared in two possible forms: one is a solution sample and the other is a thin film. *Chen* et al. made SWNT solutions by cutting and grinding the nanotube sample [41], and they successfully measured the optical absorption spectra of undoped and of doped SWNTs using a solution sample. Kataura and co-workers have developed a so called "spray method" for thin film preparation [42], whereby the soot containing SWNTs is dispersed in ethanol and then sprayed onto a quartz plate using a conventional air-brush which is normally obtained in a paint store. In this way, the thickness and the homogeneity of the thin film are controlled by the number of spraying and drying processes, but the thickness of the film ($\sim$ 300nm with 20% filling) is not precisely controlled.

In the case of the NiY catalyst, a web form of SWNTs which is predominantly in the bundle form is obtained by the electric arc method, and the resulting material can be easily purified by heating in air at 350°C for 30min and by rinsing out metal particles using hydrochloric acid. The purification is effective in removing the nanospheres (soot) and catalyst, and this is confirmed by TEM images and X-ray diffraction. The nanotube diameter distribution of the sample can be estimated by TEM observations [43,44], and the diameter distribution, thus obtained, is consistent with the distribution obtained using resonance Raman spectroscopy of the RBMs.

2.3 Diameter-Dependent Optical Absorption

In Fig. 10, the optical absorption spectra of an as-prepared and a purified SWNT thin film sample are shown, respectively, by the solid and dashed curves. Both samples are synthesized using the electric arc method and the NiY catalyst [3]. The three peaks appearing at 0.68, 1.2 and 1.7 eV correspond to the two semiconductor DOS peaks and the metallic DOS peaks discussed in the previous section. When we consider the distribution of nanotube diameters, only the first three peaks of the DOS spectra can be distinguished in relation to the calculation [45], which is consistent with the optical spectra shown in Fig. 10. Since there is no substantial difference in the spectra between the as-prepared and purified samples, we can conclude that the peaks come from the SWNTs. The dotted line denotes the photo-thermal deflection spectrum (PDS) for the same purified sample. The signal of the PDS data is proportional to the heat generated by multi-phonon processes involved in the recombination of the optically pumped electron-hole pairs, and thus the PDS spectra are considered to be free from light scattering by nano-particles [46]. Furthermore, since carbon black is used as a black body reference, the PDS reflects the difference in electronic states between SWNTs and amorphous carbon. These peak structures are more clearly seen in the PDS than in the absorption spectra, while the peak positions are almost the same as in the absorption spectra, which indicates that these peaks are not due to light scattering losses. Thus we understand that the residual nanospheres and metal

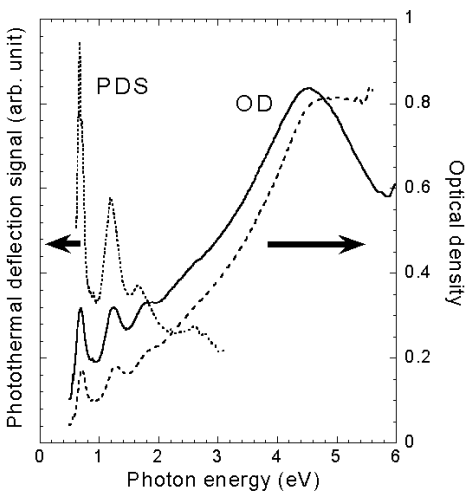

Fig. 10. Optical density in the absorption spectra of as-prepared (*solid line*) and purified (*dashed line*) SWNT thin film samples synthesized by the electric arc method using a NiY catalyst [3]. The photo-thermal deflection spectrum (PDS, *dotted line*) is also plotted for the same sample, and the spectral features of the PDS data are consistent with the absorption spectra

particles in the sample do not seriously affect the optical absorption spectrum in the energy region below 2 eV. This fact is confirmed by the observation of no change in the absorption spectra between purified and pristine samples in which the density of nanoparticles and catalysts are much different from each other.

The purified sample shows a large optical absorption band at 4.5 eV, which corresponds to the π-plasmon of SWNTs observed in the energy loss spectrum [47], which is not so clearly seen in the as-prepared sample. Figure 11 shows the optical absorption spectra of SWNTs with different diameter distributions associated with the use of four different catalysts [3]. For convenience, the large background due to the π plasmon is subtracted. The inset shows the corresponding Raman spectra of the RBMs taken with 488 nm laser excitation. The diameter distributions can be estimated from the peak frequencies using the rule, $\omega_{\mathrm{RBM}} \propto (1/d_{\mathrm{t}})$, where d_{t} is the diameter of a SWNT that is in resonance with the laser photons [5,35]. Thus, higher lying Raman

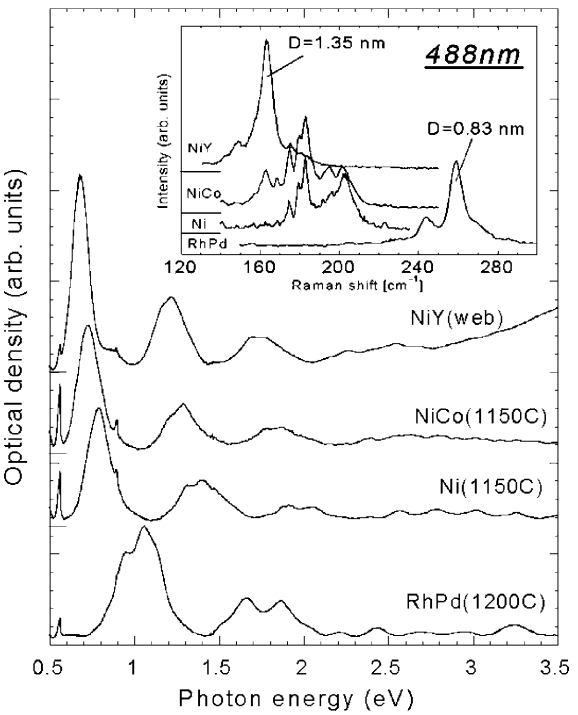

Fig. 11. Optical absorption spectra are taken for single wall nanotubes synthesized using four different catalysts, [3,4] namely NiY (1.24–1.58 nm), NiCo (1.06–1.45 nm), Ni (1.06–1.45 nm), and RhPd (0.68–1.00 nm). Peaks at 0.55 eV and 0.9 eV are due to absorption by the quartz substrate [3]. The *inset* shows the corresponding RBM modes of Raman spectroscopy obtained at 488 nm laser excitation with the same 4 catalysts

peaks indicate the presence of smaller diameter SWNTs in the sample. The nanotube diameter distribution can be estimated from the diameter d_t dependence of $\omega_{RBM} \propto 1/d_t$, once the proportionality between ω_{RBM} and *one* (n, m) nanotube is established, such as for the (10,10) nanotube. Information on the nanotube diameter distribution is available either by TEM or from measurement of the ω_{RBM} band for many laser excitation energies E_{laser}.

A method for determining $E_{11}(d_t)$ comes from optical spectra, where the measurements are made on ropes of SWNTs, so that appropriate corrections should be made for inter-tube interactions in interpreting the experimental data [29,48,49,50,51,52,53,54]. In interpreting the optical transmission data, corrections for the nonlinear k dependence of $E(k)$ away from the K-point also needs to be considered. In addition, the asymmetry of the 1D electronic density of states singularities should be taken into account in extracting the energy $E_{pp}(d_t)$ from the absorption line shape. Furthermore, the diameter distributions of the nanotubes, as well as the difference in gap energies for nanotubes of different chiralities, but for a given d_t, should be considered in the detailed interpretation of the optical transmission data to yield a value for γ_0. The calculations given in Fig. 5 provide a firm basis for a more detailed analysis.

Another important issue to address here is the so-called antenna effect of nanotubes. Since the diameter of SWNTs is much smaller than the wave length of light, an effective medium theory or other model must be used for describing the dielectric function of the nanotubes within an aligned nanotube bundle, for nanotubes that have an arbitrary polarization with respect to the randomly oriented nanotube bundles, which collectively have an anisotropic $\varepsilon_1(\omega)$ and $\varepsilon_2(\omega)$. The optical measurements should determine such fundamental properties for SWNTs.

Kazaoui et al. [24] have reported optical absorption spectra for doped SWNTs as shown in Fig. 12, including both donor (Cs) and acceptor (Br), and they found that the intensity of the absorption peaks decreased, especially for the lower energy absorption peaks with increasing dopant concentration. In the undoped SWNTs, three peaks at 0.68 eV, 1.2 eV and 1.8 eV are found in the absorption spectra in Fig. 12. When the doping concentration x in M_xC, (M = Cs, Br) is less than 0.005, the first peak at 0.68 eV decreases continuously in intensity with increasing x without changing the intensity of the second and the third peaks. In subsequent doping in the range $0.005 < x < 0.04$, the two peaks of 0.68 eV and 1.2 eV decrease in intensity. At the high doping level shown in Fig. 12b, the peak at 1.8 eV smoothes out and new bands appears at 1.07 eV and 1.30 eV for $CBr_{0.15}$ and $CCs_{0.10}$, respectively. These doping-induced absorption peaks may come from the transition between conduction to conduction inter-subband transitions and from valence to valence inter-subband transitions, respectively, for donor and acceptor type SWNTs. The difference between the peak positions 1.07 eV and 1.30 eV for acceptor and donor type SWNTs, respectively, is consistent with the expected magni-

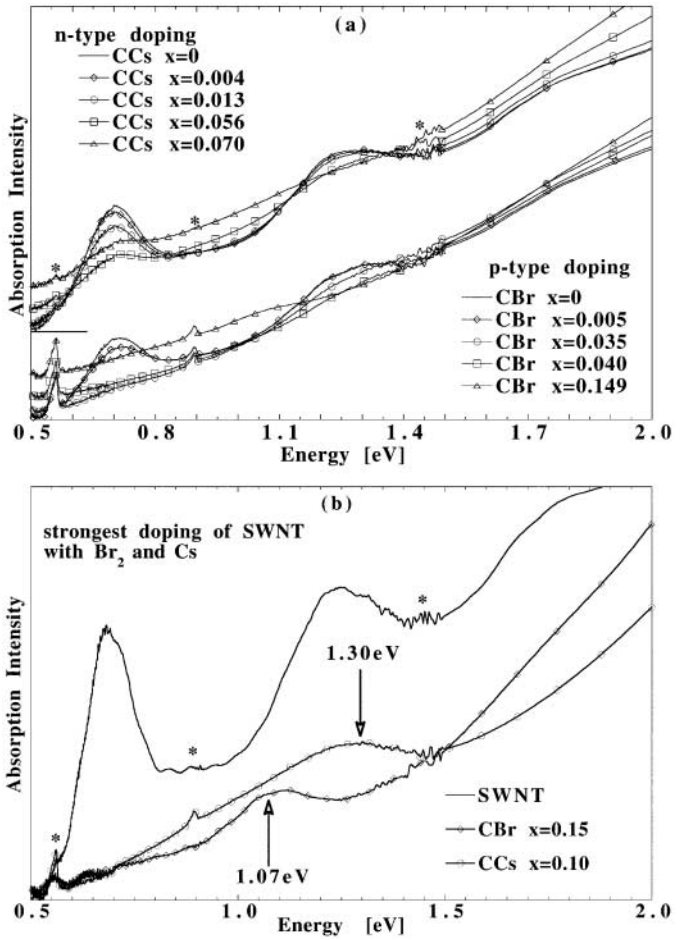

Fig. 12. (**a**) Optical absorption spectra for Cs and Br doped SWNT samples for various stoichiometries x for CCs_x and CBr_x. The entire set of spectra for the CCs_x samples is offset for clarity with a short line indicating the 0 level. * in the figure indicates features coming from the quartz substrate and from spectrometer noise. (**b**) The absorption spectra for CCs_x and CBr_x for the almost saturated doping regime [24]

tude of the asymmetry between the π and π^* bands. However, the detailed assignments for the inter-subband transitions which are responsible for the doping-induced peaks are not clear within the rigid band model.

2.4 Diameter-Dependent Resonance Raman Scattering

In the resonance Raman effect, a large scattering intensity is observed when either the incident or the scattered light is in resonance with electronic tran-

sitions between vHs in the valence and conduction bands $E_{pp}(d_t)$ for a given nanotube (n, m) [4,25,27,28,29,55,56,57,58]. In general, the size of the optical excitation beam is at least 1μm in diameter, so that many nanotubes with a large variety of (n, m) values are excited by the optical beam simultaneously, as is also the case for the optical absorption measurements discussed above. Since it is unlikely that any information on the nanotube chirality distribution is available experimentally, the assumption of equal a priori probability can be assumed, so that at a given diameter d_t the resonance Raman effect is sensitive to the width of the $E_{pp}(d_t)$ inter-subband transitions plotted in Fig. 5.

In Fig. 13 are plotted the resonance Raman spectra for SWNT samples using (a) NiY and (b) RhPd catalysts. The left and right figures for each sample (see Fig. 13) show the Raman spectra the phonon energy region of the radial breathing mode and the tangential G-bands, respectively [4]. As a first approximation, the resonant laser energy for the RBM spectra, and the G-band Raman spectra are used to estimate the $E_{pp}(d_t)$ transition energies, as shown in Fig. 5, with the diameter distribution for each catalyst. When the nanotube diameter values of $d_t = 1.24$–1.58 nm and $d_t = 0.68$–1.00 nm are used for the NiY and RhPd catalyst samples, respectively, the resonance for the metallic nanotubes $E^{M}_{pp}(d_t)$ is seen in the laser energy region around 1.6–2.0 eV and 2.4–2.8 eV, respectively. Hereafter we call this region of laser energy, which is resonant with metallic nanotubes, the "metallic window". This metallic window for the Raman RBM intensity is consistent with the optical density of the third peaks as a function of laser excitation energy, as shown in Fig. 14, where for laser excitation energies greater than 1.5 eV, the optical density (absorption) and the Raman intensity of the RBMs are consistent both for the NiY and RhPd catalyzed samples.

The metallic window for a given diameter distribution of SWNTs is obtained by the third peak of the optical absorption, as discussed in the previous subsection, and more precisely by the appearance of Raman intensity at 1540 cm^{-1} which can be seen only in the case of a rope sample containing metallic nanotubes, where the spectra are fit to a Breit–Wigner–Fano plot [4,27,28,29] as shown in Fig. 2.4.

It is pointed out here that the phonon energies of the G-band are large (0.2 eV) compared with the RBM phonon (0.02 eV), so that the resonant condition for the metallic energy window is generally different according to the difference between the RBM and G-band phonon energy. Furthermore, the resonant laser energies for phonon-emitted Stokes and phonon-absorbed anti-Stokes Raman spectra (see Sect. 2.5) are different from each other by twice the energy of the corresponding phonon. Thus when a laser energy is selected, carbon nanotubes with different diameters d_t are resonant between the RBM and G bands and between the Stokes and anti-Stokes Raman spectra, which will be described in more detail in the following subsection.

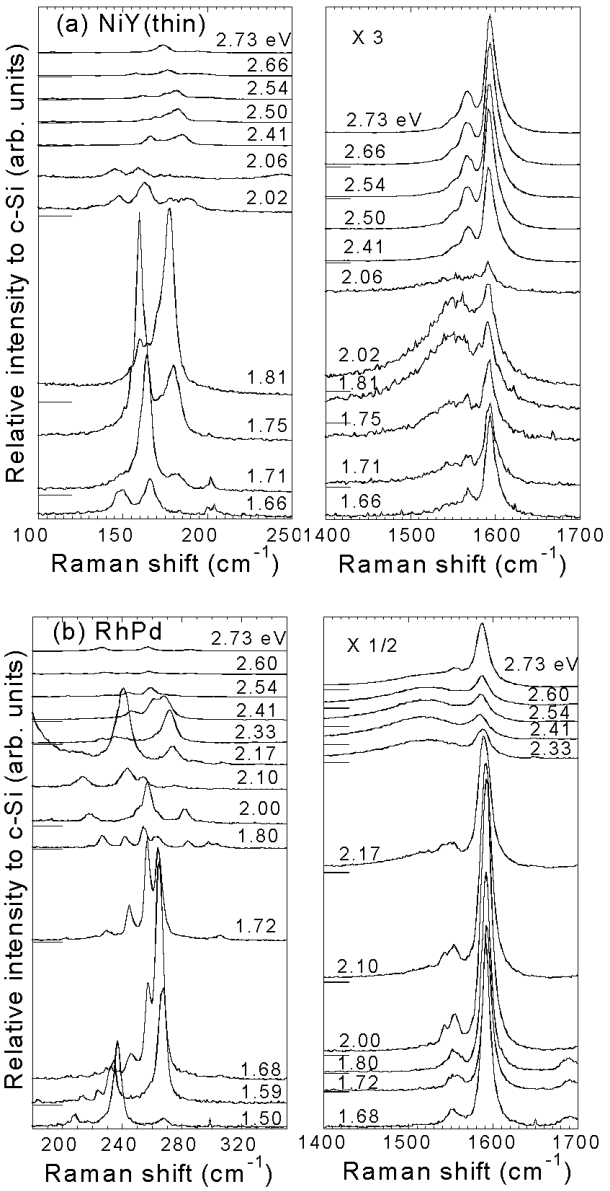

Fig. 13. Resonance Raman spectra for (**a**) NiY (*top*) and (**b**) RhPd (*bottom*) catalyzed samples. The *left* and *right* figures for each sample show Raman spectra in the phonon energy region of the RBM and the tangential G-bands, respectively [4]

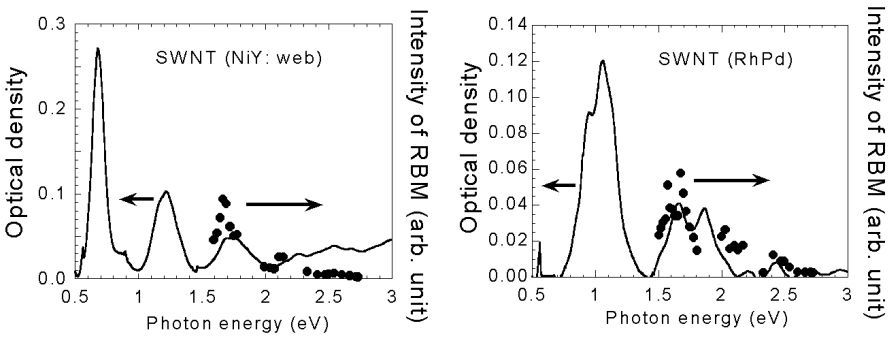

Fig. 14. Optical density of the absorption spectra (*left scale*) and the intensity of the RBM feature in the Raman spectra are plotted as a function of the laser excitation energy greater than 1.5 eV for NiY and RhPd catalyzed SWNT samples. The third peaks correspond to the metallic window [3]

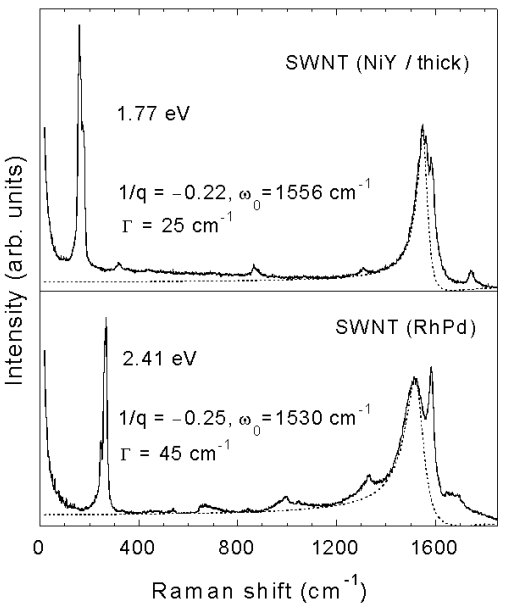

Fig. 15. Breit–Wigner–Fano plot for the Raman signals associated with the indicated G-band feature for the NiY and RhPd catalyzed samples [3]. The difference in the fitting parameters in the figures might reflect the different density of states at the Fermi level $D(E_F)$ which have been reported [59]

2.5 Stokes and Anti-Stokes Spectra in Resonant Raman Scattering

So far, almost all of the resonance Raman scattering experiments have been carried out on the Stokes spectra. The metallic window is determined experimentally as the range of E_{laser} over which the characteristic Raman spectrum for metallic nanotubes is seen, for which the most intense Raman component is at 1540 cm^{-1} [28]. Since there is essentially no Raman scattering intensity

for semiconducting nanotubes at this phonon frequency, the intensity I_{1540} provides a convenient measure for the metallic window. The normalized intensity of the dominant Lorentzian component for metallic nanotubes $\tilde{I}_{1540}$ (normalized to a reference line) has a dependence on E_{laser} given by

$$\begin{aligned}\tilde{I}_{1540}(d_0) = \sum_{d_t} A \exp\left[\frac{-(d_t - d_0)^2}{\Delta d_t^2/4}\right] \\ \times \left[(E_{11}^{\text{M}}(d_t) - E_{\text{laser}})^2 + \Gamma_e^2/4\right]^{-1} \\ \times \left[(E_{11}^{\text{M}}(d_t) - E_{\text{laser}} \pm E_{\text{phonon}})^2 + \Gamma_{\text{e}}^2/4\right]^{-1},\end{aligned} \tag{19}$$

where d_0 and $\Delta\, d_t$ are, respectively, the mean diameter and the width of the Gaussian distribution of nanotube diameters within the SWNT sample, E_{phonon} is the average energy (0.197 eV) of the tangential phonons and the $+$ $(-)$ sign in (19) refers to the Stokes (anti-Stokes) process, Γ_{e} is a damping factor that is introduced to avoid a divergence of the resonant denominator, and the sum in Eq. (19) is carried out over the nanotube diameter distribution. Equation (19) indicates that the normalized intensity for the Stokes process $\tilde{I}_{1540}^{S}(d_0)$ is large when either the incident laser energy is equal to $E_{11}^{\text{M}}(d_t)$ or when the scattered laser energy is equal to $E_{11}^{\text{M}}(d_t)$ and likewise for the anti-Stokes process. Since the phonon energy is on the same order of magnitude as the width of the metallic window for nanotubes with diameters d_t, the Stokes and the anti-Stokes processes can be observed at different resonant laser energies in the resonant Raman experiment. The dependence of the normalized intensity $\tilde{I}_{1540}(d_0)$ for the actual SWNT sample on E_{laser} is primarily sensitive [27,28,29] to the energy difference $E_{11}^{\text{M}}(d_t)$ for the various d_t values in the sample, and the resulting normalized intensity $\tilde{I}_{1540}(d_0)$ is obtained by summing over d_t.

In Fig. 16 we present a plot of the expected integrated intensities $\tilde{I}_{1540}(d_0)$ for the resonant Raman process for metallic nanotubes for both the Stokes (solid curve) and anti-Stokes (square points) processes. This figure is used to distinguishes 4 regimes for observation of the Raman spectra for Stokes and anti-Stokes processes shown in Fig. 17: (1) the semiconducting regime (2.19 eV), for which both the Stokes and anti-Stokes spectra receive contributions from semiconducting nanotubes, (2) the metallic regime (1.58 eV), where metallic nanotubes contribute to both the Stokes and anti-Stokes spectra, (3) the regime (1.92 eV), where metallic nanotubes contribute to the Stokes spectra and not to the anti-Stokes spectra, and (4) the regime (1.49 eV), where the metallic nanotubes contribute only to the anti-Stokes spectra and not to the Stokes spectra. The plot in Fig. 16 is for a nanotube diameter distribution $d_t = 1.49 \pm 0.20$ nm assuming $\gamma_{\text{e}} = 0.04$ eV. Equation (17) can be used to determine γ_0 from the intersection of the Stokes and anti-Stokes curves at 1.69 eV in Fig. 16, yielding a value of $\gamma_0 = 2.94 \pm 0.05$ eV [55,60].

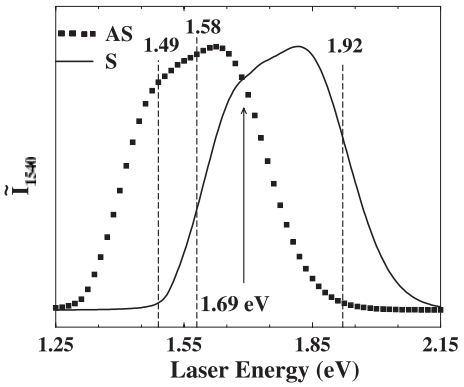

Fig. 16. Metallic window for carbon nanotubes with diameter of $d_t = 1.49 \pm 0.20$ nm for the Stokes (*solid line*) and anti-Stokes (*square points*) processes plotted in terms of the normalized intensity of the phonon component at 1540 cm^{-1} for metallic nanotubes vs the laser excitation energy for the Stokes and the anti-Stokes scattering processes [60]. The crossing between the Stokes and anti-Stokes curves is denoted by the *vertical arrow*, and provides a sensitive determination of γ_0 [55,60]

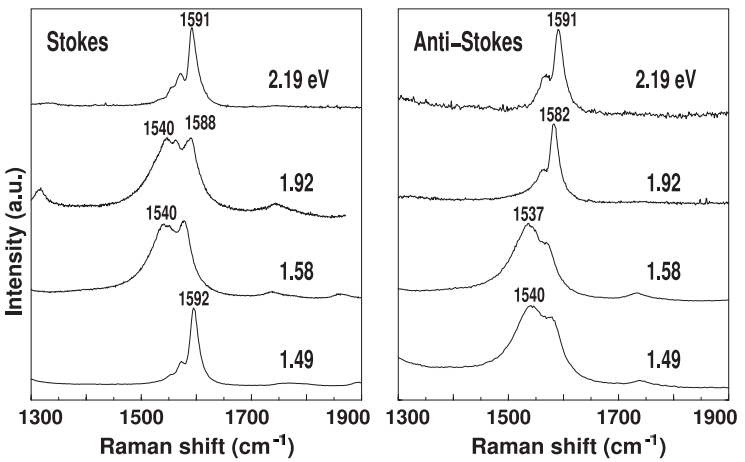

Fig. 17. Resonant Raman spectra for the Stokes and anti-Stokes process for SWNTs with a diameter distribution $d_t = 1.49 \pm 0.20$ nm [60]

2.6 Bundle Effects on the Optical Properties of SWNTs (Fano Effect)

Although the origin of the 1540 cm^{-1} Breit–Wigner–Fano peak is not well explained, the Fano peaks are relevant to the bundle effect which is discussed in this subsection. This idea can be explained by the Raman spectra observed for the Br_2 doped SWNT sample. The frequency of the RBMs are shifted upon doping, and from this frequency shift the charge transfer of the electrons from

the SWNTs to the Br_2 molecules can be measured [61]. This charge transfer enhances the electrical conductivity whose temperature dependence shows metallic behavior [62]. When SWNTs made by the arc method with the NiY catalyst are used, the undoped SWNT sample exhibits the RBM features around 170 cm^{-1}. When the SWNTs are doped by Br_2 molecules, new RBM peaks appear at around 240 cm^{-1} when the laser excitation energy is greater than 1.8 eV, as shown in Fig. 18a. When the Raman spectra for the fully Br_2 doped sample are measured, new features at 260 cm^{-1} are observed, but the peak at 260 cm^{-1} disappears and a new peak at 240 cm^{-1} can be observed for laser excitation energy greater than 1.96 eV (see Fig. 18) when the sample chamber is evacuated at room temperature, and the spectra for the undoped SWNTs are observed showing RBM peaks around 170 cm^{-1}. Since heating in vacuum up to 250°C is needed to remove the bromine completely, the evacuated sample at room temperature consists of a partially doped bundle and an easily undoped portion, which is identified with isolated SWNTs, not in bundles. Since the Fermi energy shifts downward in the acceptor-doped portion of the sample, no resonance Raman effect is expected in the excitation

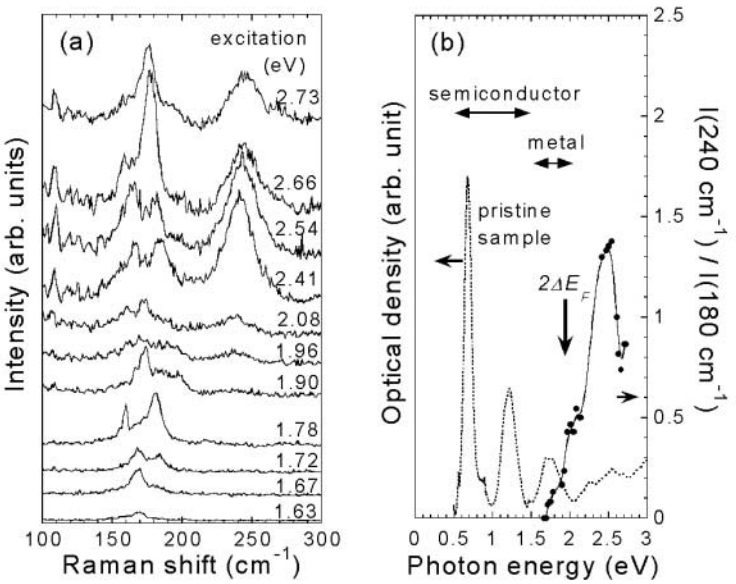

Fig. 18. (**a**) Resonance Raman spectra for bromine doped SWNTs prepared using a NiY catalyst. The sample is evacuated after full doping at room temperature. An additional peak around 240 cm^{-1} can be seen for laser excitation energies greater than 1.96 eV. (**b**) (*left scale*) The optical density of the absorption spectra for pristine (undoped) SWNT samples and (*right scale*) the intensity ratio of the RBMs at ∼240 cm^{-1} appearing only in the doped samples to the RBM at ∼180 cm^{-1} for the undoped sample. The additional RBM peaks appear when the metallic window is satisfied [63]

energy range corresponding to the semiconductor first and second peaks and the metallic third peak in the optical absorption spectra. In fact, in Fig. 18b, the intensity ratio of the Raman peaks around 240 cm^{-1} to that at 180 cm^{-1} is plotted by solid circles and the curve connecting these points is shown in the figure as a function of laser excitation energy. Also shown in the figure is the corresponding optical absorption spectrum for the pristine (undoped) sample plotted by the dotted curve. The onset energy of the Raman peaks at 240 cm^{-1} is consistent with the energy $2\Delta E_F$ which corresponds to the energy of the third metallic peak of the optical absorption. In fact, the optical absorption of the three peaks disappear upon Br_2 doping (Fig.12) [24,41]. The peaks of Raman intensity at 240 cm^{-1} are relevant to resonant Raman scattering associated with the fourth or the fifth broad peaks of doped semiconductor SWNTs.

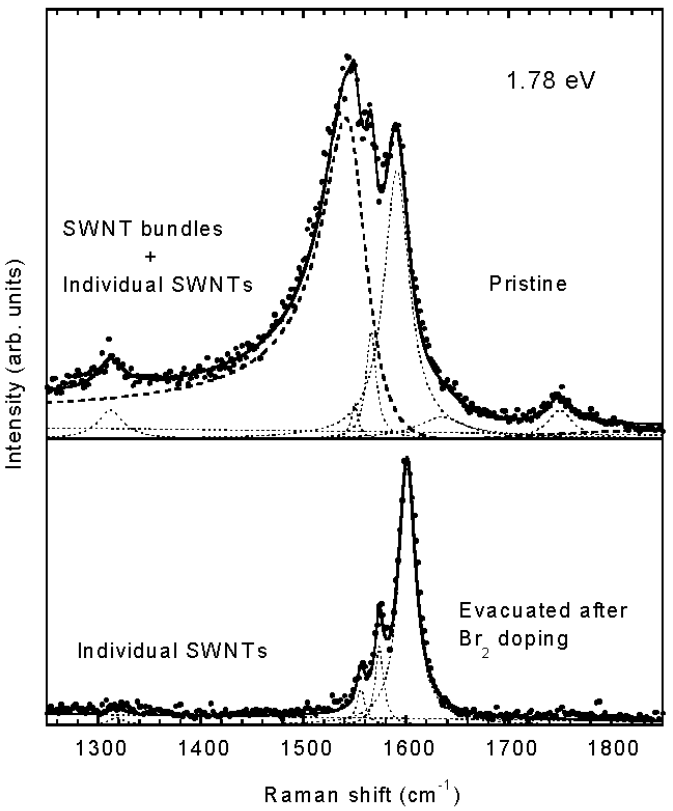

Fig. 19. The Raman Spectra for the undoped sample (*top*) and for the evacuated sample (*bottom*) after full Br_2 doping at room temperature. The Fano spectral feature at 1540 cm^{-1} is missing in the spectrum for the evacuated sample [63]

For this evacuated sample, the G-band spectra with the laser energy 1.78 eV is shown in Fig. 19. This laser energy corresponds to an energy in the metallic window, but no resonance Raman effect is expected from the doped bundle portion, as discussed above. Thus the resonant Raman spectra should be observed only in metallic nanotubes in the undoped portion of the sample which is considered to contain only isolated SWNTs. Surprisingly there are no 1540 cm^{-1} Fano-peaks for such an evacuated sample, although the undoped sample has a mixture 1590 cm^{-1} and 1540 cm^{-1} peaks, as shown in Fig. 19 for comparison. Thus it is concluded that the origin of the 1540 cm^{-1} peaks is relevant to the nanotubes located within bundles. The interlayer interaction between layers of SWNTs is considered to be on the order of 5–50 cm^{-1} [29,48,49,50,52,53,54] and thus the difference between 1590 cm^{-1} and 1540 cm^{-1} is of about the same order of magnitude as the interlayer interaction. One open issue awaiting solution is why the 1540 cm^{-1} peaks are observed only when the metallic nanotube is within a bundle, and when the laser excitation is within the metallic window and corresponds to an interband transition contributing to the optical absorption. Thus the mechanism responsible for the 1540 cm^{-1} peak is not understood from a fundamental standpoint.

2.7 Resonance Raman Scattering of MWNTs

Multi-walled carbon nanotubes (MWNTs) prepared by the carbon arc method are thought to be composed of a coaxial arrangement of concentric nanotubes. For example, ^{13}C-NMR [64] and magnetoresistance measurements [65,66] show Aharonov–Bohm effects that are associated with the concentric tube structures. On the other hand, the thermal expansion measurements [67] and the doping effects [68] suggest that some kinds of MWNTs have scroll structures. If the RBMs, which are characteristic of SWNTs [35], are observed in MWNTs, the RBM Raman spectra might provide experimental evidence for the coaxial structure. In many cases, however, MWNTs have very large diameters compared with SWNTs even for the innermost layer of the nanotube, and no one has yet succeeded in observing the RBMs in large diameter MWNTs. Zhao and Ando have succeeded in synthesizing MWNTs with an innermost layer having a diameter less than 1.0 nm, by using an electric arc operating in hydrogen gas [69]. The spectroscopic observations on this sample revealed many Raman peaks in the low frequency region, which these RBM frequencies can be used to assign (n, m) values for some constituent layers of MWNTs [70]. Since the resonance Raman effect can be observed in MWNTs (see Fig. 20), we can be confident that these low frequency features are associated with RBMs.

Several MWNT samples have been prepared by the carbon arc method using a range of hydrogen pressures from 30 to 120 Torr, and yielding good MWNT samples under all of these operating conditions. Relative yields depend on the hydrogen pressure and on the arc current [69], with the highest

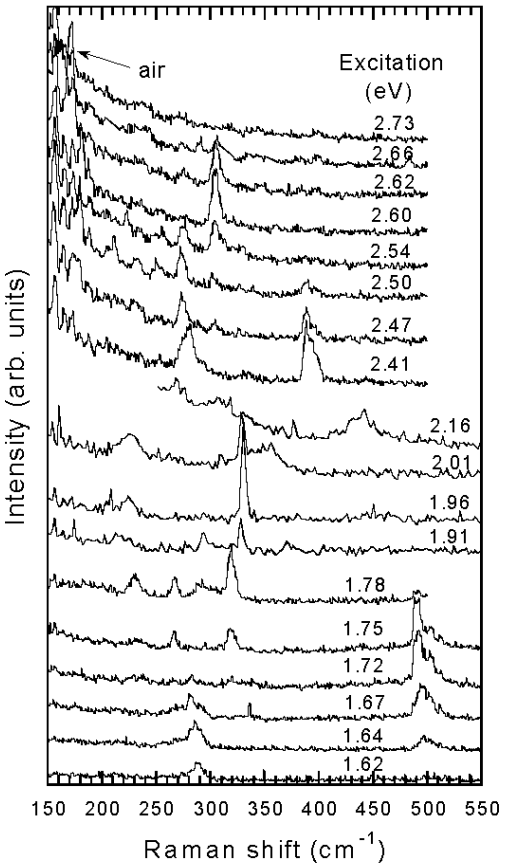

Fig. 20. The resonant Raman spectra of multi-wall carbon nanotubes with very small innermost diameters that grow preferentially using an electric arc in hydrogen gas [71]

yield of MWNTs being obtained at 60 Torr of hydrogen gas pressure. The sample purity, after purification of the sample, which was characterized using an infrared lamp, is over 90% MWNTs and the diameter distribution of the innermost shell was measured by TEM. Most of the MWNTs have diameters of the innermost shell of about 1.0 nm, and sometimes innermost diameters less than 0.7 nm were observed.

In Fig. 20 resonance Raman scattering of samples synthesized under different conditions have been measured, and RBM peaks have been observed from 200 to 500 cm^{-1}[63]. Peaks between 150 and 200 cm^{-1} are due to the air. In fact these peaks of O_2 and N_2 are commonly observed not only for the MWNT sample but also for the quartz substrate and they are not observed in Ar gas. Peaks above 200 cm^{-1} show very sharp resonances, which strongly suggest that these structures originate from the RBM vibrations of nanotubes. Resonance effects for each peak are similar to those of single-walled nanotubes. However, the peak frequencies are about 5% higher than those of single-walled nanotubes with the same diameter, which might be due to

the inter-layer interaction. For example, the RBM peak at 280 cm^{-1} shows a maximum intensity at 2.41 eV. This is the same behavior as the peak at 268 cm^{-1} in SWNTs. This fact is consistent with the recent calculation of bundle effects on the RBM frequency of SWNTs which predict a 10% upshift in the mode frequency due to tube–tube interactions [53]. From the simple relationship between nanotube diameter and RBM frequency [35], the candidate nanotube shells for the peak at 490 cm^{-1} are (5,1), (6,0), (4,3) and (5,2) having RBM frequencies at 509.6, 472.8, 466.4 and 454.3 cm^{-1}, respectively. If we take into account the 5% up-shift due to the interlayer interactions, the candidates are narrowed down to the nanotube shells (6,0), (4,3) and (5,2), which have diameters of 0.470, 0.477 and 0.489 nm, respectively, and these diameters are consistent with the TEM observations. It is very interesting that the (6,0) nanotube has the same structure as D_{6h} C_{36} which has D_{6h} symmetry [72]. However, we also have to consider the electronic states of the nanotube to clearly identify the resonance effect. By use of the zone-folding band calculation [2,8,16], assuming a transfer integral $\gamma_0 = 2.75$ eV, it is found that (6,0) and (5,2) are metallic nanotubes and have their lowest energy gap E_{11}^{M} at 4.0 eV. The resonance laser energy, where the RBM peak has a maximum intensity, occurs at 1.7 eV, and the peak at 490 cm^{-1} was assigned to the (4,3) nanotube which is a semiconductor, and has its lowest energy gap E_{11}^{S} at 1.6 eV. In the same way, the candidates (7,1) and (5,4) were considered for the Raman band at 388 cm^{-1}. The nanotube (7,1) is metallic and the lowest energy gap E_{11}^{M} is at 3.4 eV, while the (5,4) nanotube should be semiconducting and is expected to have E_{11}^{S} and E_{22}^{S} at 1.28 and 2.52 eV, respectively. Thus, the peak at 388 cm^{-1} should be assigned to the nanotube shell (5,4) because of the resonance observed at 2.4 eV[71].

Finally we consider the interlayer interactions in MWNTs. The RBM band in Fig. 20 at 490 cm^{-1} is split into three peaks indicating the same resonance feature. These peaks cannot be explained by different nanotubes, since there are no other candidates available. The nanotube (5,1) is the only candidate having the nearest diameter and the nearest energy gap in the optical spectra. However, the calculated energy gap of a (5,1) nanotube is 1.7 eV, which is 0.1 eV wider than that for a (4,3) nanotube. If one of the peaks originates from a (5,1) nanotube, the resonance feature should be different from that for the other peaks. Further, the RBM frequency of a (5,1) nanotube becomes 534 cm^{-1}, taking into account the 5% up-shift due to the inter-tube interaction in a nanotube bundle. Thus, it is proper to think that these three peaks are originating from the same nanotube. The possible reason for the splitting of this peak is the interlayer interaction. When the first layer is (4,3), then (10,7) is the best selection as the second layer, since the interlayer distance is 0.342 nm, which is a typical value for MWNTs [73]. The other nearest candidates for the second layers are (13,3), (9,8) and (11,6) having inter-layer distances 0.339, 0.339 and 0.347 nm, respectively. The interlayer distance for the (13,3) and (9,8) candidates are about the same (about 1% smaller) as

the typical inter-layer distance, and but the interlayer distance for the (11,6) nanotube is 1.5% larger. The magnitude of the interlayer interaction should depend on the interlayer distance, and, consequently, the RBM frequency of the first layer may depend on the chiral index of the second layer. Indeed, the observed frequency separation between the split peaks is about 2%, which may be consistent with the difference in interlayer distances. The splitting into three RBM probably indicates that there are at least three kinds of second layers. Furthermore, this splitting cannot be explained by a scrolled structure for MWNTs. This strongly suggests that the MWNTs fabricated by the electric arc operating in hydrogen gas has a concentric structure. For the thinnest nanotube (4,3), the RBM frequency of the second layer is 191 cm^{-1}. This should be the highest RBM frequency of the second layer nanotube. Since the low frequency region is affected by signals from the air, Raman spectra were taken while keeping the sample in argon gas. However, no peak was observed below 200 cm^{-1}, suggesting that only the innermost nanotube has a significant Raman intensity. The innermost layer has only an outer nanotube as a neighbor, while the other nanotubes, except for the outermost layer, have both inner and outer nanotube neighbors.

The interlayer interaction probably broadens the one-dimensional band structure, in a like manner to the bundle effect in SWNTs [48,49,50,51,52,29] [53,54]. The band broadening decreases the magnitude of the joint density of states at the energy gap, leading to a decrease in the resonant Raman intensity of the second layer. On the other hand, the RBM frequency of the outermost layer is too low to measure because of its large diameter. Thus, RBMs are observed in MWNTs only for the innermost nanotubes. Theoretical calculations show that SWNTs with diameters smaller than C_{60} show metallic behavior because of the hybridization effect of the $2p_z$ orbital with that of the σ electron [74,75]. The hybridization effect lowers the energy of the conduction band and raises the energy of the valence band, which results in the semi-metallic nature of the electronic states. However, the electrostatic-conductance of two-probe measurement of MWNTs shows that semiconducting nanotubes seems to be dominant in this diameter region[76]. Thus it is necessary to investigate the electronic properties of SWNTs with diameters smaller than that of C_{60}.

3 Summary

In summary, the spectra of the DOS for SWNTs have a strong chirality dependence. Especially for metallic nanotubes, the DOS peaks are found to be split into two peaks because of the trigonal warping effect, while semiconducting nanotubes do not show a splitting. The width of the splitting becomes a maximum for the metallic zigzag nanotubes $(3n, 0)$, and is zero for armchair nanotubes (n, n), which are always metallic. In the case of semiconducting nanotubes, the upper and lower bounds of the peak positions of $E_{11}^{\mathrm{S}}(d_{\mathrm{t}})$ on the Kataura chart shown in Fig. 5 are determined by the values of $E_{11}^{\mathrm{S}}(d_{\mathrm{t}})$ for

the $(3n+1,0)$ or $(3n-1,0)$ zigzag nanotubes. The upper and lower bounds of the widths of the $E_{ii}^{\mathrm{S}}(d_{\mathrm{t}})$ curves alternate with increasing i between the $(3n+1,0)$ and $(3n-1,0)$ zigzag nanotubes.

The existence of a splitting of the DOS spectra for metallic nanotubes should depend on the chirality which should be observable by STS/STM experiments, consistent with the experiments of *Kim* et al. [22]. The width of the metallic window can be observed in resonant Raman experiments, especially through the differences between the analysis for the Stokes and the anti-Stokes spectra. Some magnetic effects should be observable in the resonant Raman spectra because an applied magnetic field should perturb the 1D DOS for the nanotubes, since the magnetic field will break the symmetry between the K and K' points. The magnetic susceptibility, which has been important for the determination of γ_0 for 3D graphite [77,78], could also provide interesting results regarding a determination of $E_{pp}(d_{\mathrm{t}})$ for SWNTs, including the dependence of $E_{pp}(d_{\mathrm{t}})$ on d_{t}.

Purification of SWNTs to provide SWNTs with a known diameter and chirality should be given high priority for future research on carbon nanotube physics. Furthermore, we can anticipate future experiments on SWNTs which could illuminate phenomena showing differences in the $E(k)$ relations for the conduction and valence bands of SWNTs. Such information would be of particular interest for the experimental determination of the overlap integral s as a function of nanotube diameter. The discussion presented in this article for the experimental determination of $E_{pp}(d_{\mathrm{t}})$ depends on assuming $s=0$, in order to make direct contact with the tight-binding calculations. However, if $s \neq 0$, then the determination of $E_{pp}(d_{\mathrm{t}})$ would depend on the physical experiment that is used for this determination, because different experiments emphasize different k points in the Brillouin zone. The results of this article suggest that theoretical tight binding calculations for nanotubes should also be refined to include the effect of $s \neq 0$. Higher order (more distant neighbor) interactions should yield corrections to the lowest order theory discussed here.

The $1540\,\mathrm{cm}^{-1}$ feature appears only in the Raman spectra for a metallic bundle, but not for semiconducting SWNTs nor for individual metallic SWNTs. The inter-tube interaction in MWNTs gives 5% higher RBM mode frequencies than in SWNT bundles, and the intertube-interaction effect between the MWNT innermost shell and its adjacent outer shell is important for splitting the RBM peaks of a MWNT sample.

Acknowledgments

The authors gratefully acknowledge stimulating and valuable discussions with Profs. M.S. Dresselhaus and G. Dresselhaus for the writing of this chapter. R.S. and H.K. acknowledge a grant from the Japanese Ministry of Education (No. 11165216 and No. 11165231), respectively. R.S. acknowledges support from the Japan Society for the Promotion of Science for his visit to MIT.

H.K. acknowledges the Japan Society for Promotion of Science Research for support for the Future Program.

References

1. M. S. Dresselhaus, G. Dresselhaus, P. C. Eklund, *Science of Fullerenes and Carbon Nanotubes* (Academic, New York 1996) 213, 214
2. R. Saito, G. Dresselhaus, M. S. Dresselhaus, *Physical Properties of Carbon Nanotubes* (Imperial College Press, London, 1998) 213, 214, 215, 216, 217, 218, 224, 241
3. H. Kataura, Y. Kumazawa, Y. Maniwa, I. Umezu, S. Suzuki, Y. Ohtsuka, Y. Achiba, Synth. Met. **103**, 2555 (1999) 213, 220, 227, 228, 229, 234
4. H. Kataura, Y. Kumazawa, N. Kojima, Y. Maniwa, I. Umezu, S. Masubuchi, S. Kazama, X. Zhao, Y. Ando, Y. Ohtsuka, S. Suzuki, Y. Achiba In *Proc. of the Int. Winter School on Electronic Properties of Novel Materials (IWEPNM'99)*, H. Kuzmany, M. Mehring, J. Fink (Eds.) (American Institute of Physics, Woodbury 1999) AIP Conf. Proc. (in press) 213, 219, 220, 229, 232, 233
5. S. Bandow, S. Asaka, Y. Saito, A. M. Rao, L. Grigorian, E. Richter, P. C. Eklund, Phys. Rev. Lett. **80**, 3779 (1998) 213, 225, 229
6. J. C. Charlier and S. Iijima, Chapter 4 in this volume 213
7. M. S. Dresselhaus, G. Dresselhaus, R. Saito, Phys. Rev. B **45**, 6234 (1992) 214
8. R. Saito, M. Fujita, G. Dresselhaus, M. S. Dresselhaus, Phys. Rev. B **46**, 1804 (1992) 216, 218, 241
9. G. S. Painter, D. E. Ellis, Phys. Rev. B **1**, 4747 (1970) 216
10. M. S. Dresselhaus, G. Dresselhaus, K. Sugihara, I. L. Spain, H. A. Goldberg, *Graphite Fibers and Filaments* , Vol. 5, *Springer Ser. Mater. Sci.* (Springer, Berlin, Heidelberg 1988) 216, 225
11. R. Saito, G. Dresselhaus, M. S. Dresselhaus, Phys. Rev. B **61**, 2981 (2000) 217, 220, 222
12. P. R. Wallace, Phys. Rev. **71**, 622 (1947) 216
13. J. W. McClure, Phys. Rev. **104**, 666 (1956) 216
14. R. A. Jishi, D. Inomata, K. Nakao, M. S. Dresselhaus, G. Dresselhaus, J. Phys. Soc. Jpn. **63**, 2252 (1994) 217, 218, 224
15. N. Hamada, S. Sawada, A. Oshiyama, Phys. Rev. Lett. **68**, 1579 (1992) 218
16. R. Saito, M. Fujita, G. Dresselhaus, M. S. Dresselhaus, Appl. Phys. Lett. **60**, 2204 (1992) 218, 241
17. K. Tanaka, K. Okahara, M. Okada, T. Yamabe, Chem. Phys. Lett. **191**, 469 (1992) 218
18. J. W. G. Wildöer, L. C. Venema, A. G. Rinzler, R. E. Smalley, C. Dekker, Nature (London) **391**, 59 (1998) 219
19. T. W. Odom, J. L. Huang, P. Kim, C. M. Lieber, Nature (London) **391**, 62 (1998) 219
20. T. W. Odom, J. L. Huang, P. Kim, M. Ouyang, C. M. Lieber, J. Mater. Res. **13**, 2380 (1998) 219
21. T. W. Odom, Private communication 219
22. P. Kim, T. Odom, J.-L. Huang, C. M. Lieber, Phys. Rev. Lett. **82**, 1225 (1999) 219, 222, 224, 243
23. H. Ajiki, T. Ando, Physica B, Condensed Matter **201**, 349 (1994) 219, 220

24. S. Kazaoui, N. Minami, R. Jacquemin, H. Kataura, Y. Achiba, Phys. Rev. B **60**, 13339 (1999) 219, 230, 231, 238
25. A. M. Rao, E. Richter, S. Bandow, B. Chase, P. C. Eklund, K. W. Williams, M. Menon, K. R. Subbaswamy, A. Thess, R. E. Smalley, G. Dresselhaus, M. S. Dresselhaus, Science **275**, 187 (1997) 219, 222, 224, 232
26. A. Kasuya, Y. Sasaki, Y. Saito, K. Tohji, Y. Nishina, Phys. Rev. Lett. **78**, 4434 (1997) 219, 226
27. M. A. Pimenta, A. Marucci, S. D. M. Brown, M. J. Matthews, A. M. Rao, P. C. Eklund, R. E. Smalley, G. Dresselhaus, M. S. Dresselhaus, J. Mater. Res. **13**, 2396 (1998) 219, 222, 232, 235
28. M. A. Pimenta, A. Marucci, S. Empedocles, M. Bawendi, E. B. Hanlon, A. M. Rao, P. C. Eklund, R. E. Smalley, G. Dresselhaus, M. S. Dresselhaus, Phys. Rev. B **58**, R16016 (1998) 219, 222, 232, 234, 235
29. L. Alvarez, A. Righi, T. Guillard, S. Rols, E. Anglaret, D. Laplaze, J.-L. Sauvajol, Chem. Phys. Lett. **316**, 186 (2000) 219, 222, 230, 232, 235, 239, 242
30. J. W. Mintmire, C. T. White, Phys. Rev. Lett. **81**, 2506 (1998) 219
31. C. T. White, T. N. Todorov, Nature (London) **393**, 240 (1998) 219
32. S. J. Tans, R. M. Verschueren, C. Dekker, Nature **393**, 49 (1998) 222
33. P. Lambin, Private communication 222
34. J. Yu, K. Kalia, P. Vashishta, Europhys. Lett. **32**, 43 (1995) 224
35. R. Saito, T. Takeya, T. Kimura, G. Dresselhaus, M. S. Dresselhaus, Phys. Rev. B **57**, 4145 (1998) 224, 225, 226, 229, 239, 241
36. O. Madelung, *Solid State Theory* (Springer, Berlin, Heidelberg 1978) 224
37. R. Saito, G. Dresselhaus, M. S. Dresselhaus, In *Science and Technology of Carbon Nanotubes*, K. Tanaka, T. Yamabe, K. Fukui (Eds.), (Elsevier Science Ltd., Oxford 1999) pp. 51–62 224
38. S. Guha, J. Menéndez, J. B. Page, G. B. Adams, Phys. Rev. B **53**, 13106 (1996) 226
39. M. J. Matthews, M. A. Pimenta, G. Dresselhaus, M. S. Dresselhaus, M. Endo, Phys. Rev. B **59**, R6585 (1999) 226
40. H. Kataura, A. Kimura, Y. Ohtsuka, S. Suzuki, Y. Maniwa, T. Hanyu, Y. Achiba, Jpn. J. Appl. Phys. **37**, L616 (1998) 227
41. J. Chen, M. A. Hamon, H. Hu, Y. Chen, A. M. Rao, P. C. Eklund, R. C. Haddon, Science **282**, 95 (1998) 227, 238
42. H. Kataura. (unpublished) 227
43. S. Iijima, T. Ichihashi, Nature (London) **363**, 603 (1993) 227
44. D. S. Bethune, C. H. Kiang, M. S. de Vries, G. Gorman, R. Savoy, J. Vazquez, R. Beyers, Nature (London) **363**, 605 (1993) 227
45. M. Ichida, J. Phys. Soc. Jpn. **68**, 3131 (1999) 228
46. I. Umezu, M. Daigo, K. Maeda, Jpn. J. Appl. Phys. **33**, L873 (1994) 228
47. T. Pichler, M. Knupfer, M. S. Golden, J. Fink, A. Rinzler, R. E. Smalley, Phys. Rev. Lett. **80**, 4729 (1998) 229
48. J.-C. Charlier, J. P. Michenaud, Phys. Rev. Lett. **70**, 1858 (1993) 230, 239, 242
49. J.-C. Charlier, X. Gonze, J. P. Michenaud, Europhys. Lett. **29**, 43 (1995) 230, 239, 242
50. E. Richter, K. R. Subbaswamy, Phys. Rev. Lett. **79**, 2738 (1997) 230, 239, 242
51. Y. K. Kwon, S. Saito, D. Tománek, Phys. Rev. B **58**, R13314 (1998) 230, 242
52. U. D. Venkateswaran, A. M. Rao, E. Richter, M. Menon, A. Rinzler, R. E. Smalley, P. C. Eklund, Phys. Rev. B **59**, 10928 (1999) 230, 239, 242

53. L. Henrard, E. Hernández, P. Bernier, A. Rubio, Phys. Rev. B **60**, R8521 (1999) 230, 239, 241, 242
54. D. Kahn, J. P. Lu, Phys. Rev. B **60**, 6535 (1999) 230, 239, 242
55. G. Dresselhaus, M. A. Pimenta, R. Saito, J.-C. Charlier, S. D. M. Brown, P. Corio, A. Marucci, M. S. Dresselhaus, in *Science and Applications of Nanotubes*, D. Tománek, R. J. Enbody (Eds.), (Kluwer Academic, New York 2000) pp. 275–295 232, 235, 236
56. M. S. Dresselhaus, M. A. Pimenta, K. Kneipp, S. D. M. Brown, P. Corio, A. Marucci, G. Dresselhaus, in *Science and Applications of Nanotubes*, D. Tománek, R. J. Enbody (Eds.), (Kluwer Academic, New York 2000) pp. 253–274 232
57. A. Kasuya, M. Sugano, Y. Sasaki, T. Maeda, Y. Saito, K. Tohji, H. Takahashi, Y. Sasaki, M. Fukushima, Y. Nishina, C. Horie, Phys. Rev. B **57**, 4999 (1998) 232
58. M. Sugano, A. Kasuya, K. Tohji, Y. Saito, Y. Nishina, Chem. Phys. Lett. **292**, 575 (1998) 232
59. X. P. Tang, A. Kleinhammes, H. Shimoda, L. Fleming, K. Y. Bennoune, C. Bower, O. Zhou, Y. Wu, MRS Proc. **593**, J. Robertson, J. P. Sullivan, O. Zhou, T. B. Allen, B. F. Coll (Eds.), (2000) 234
60. S. D. M. Brown, P. Corio, A. Marucci, M. S. Dresselhaus, M. A. Pimenta, K. Kneipp, Phys. Rev. B **61**, R5137 (2000) 235, 236
61. A. M. Rao, P. C. Eklund, S. Bandow, A. Thess, R. E. Smalley, Nature (London) **388**, 257 (1997) 237
62. R. S. Lee, H. J. Kim, J. E. Fischer, A. Thess, R. E. Smalley, Nature (London) **388**, 255 (1997) 237
63. H. Kataura, Y. Kumazawa, N. Kojima, Y. Maniwa, I. Umezu, S. Masubuchi, S. Kazama, Y. Ohtsuka, S. Suzuki, Y. Achiba, Mol. Cryst. Liquid Cryst.0 (2000) 237, 238, 240
64. Y. Maniwa, M. Hayashi, Y. Kumazawa, H. Tou, H. Kataura, H. Ago, Y. Ono, T. Yamabe, K. Tanaka, AIP Conf. Proc. **442**, 87 (1998) 239
65. A. Fujiwara, K. Tomiyama, H. Suematsu, M. Yumura, K. Uchida, Phys. Rev. B **60**, 13492 (1999) 239
66. A. Bachtold, C. Strunk, J. P. Salvetat, J. M. Bonard, L. Forró, T. Nussbaumer, C. Schönenberger, Nature **397**, 673 (1999) 239
67. S. Bandow, Jpn J. Appl. Phys. **36**, L1403 (1997) 239
68. V. Z. Mordkovich, Mol. Cryst. Liquid Cryst. (2000) 239
69. X. Zhao, M. Ohkohchi, M. Wangm, S. Iijima, T. Ichihashi, Y. Ando, Carbon **35**, 775 (1997) 239
70. X. Zhao, Y. Ando, Jpn. J. Appl. Phys. **37**, 4846 (1998) 239
71. H. Kataura, Y. Achiba, X. Zhao, Y. Ando, In *MRS Symp. Proc., Boston, Fall 1999*, J. Robertson, J. P. Sullivan, O. Zhou, T. B. Allen, B. F. Coll (Eds.) (Materials Research Society Press, Pittsburgh, PA 2000) 240, 241
72. C. Piskoti, J. Yarger, A. Zettl, Nature **393**, 771 (1998) 241
73. Y. Saito, T. Yoshikawa, S. Bandow, M. Tomita, T. Hayashi, Phys. Rev. B **48**, 1907 (1993) 241
74. X. Blase, L. X. Benedict, E. L. Shirley, S. G. Louie, Phys. Rev. Lett. **72**, 1878 (1994) 242
75. S. G. Louie, chapter 6 in this volume 242
76. K. Kaneto, M. Tsuruta, G. Sakai, W. Y. Cho, Y. Ando, Synth. Met. **103**, 2543 (1999) 242

77. J. W. McClure, Phys. Rev. **108**, 612 (1957) 243
78. K. S. Krishnan, Nature (London) **133**, 174 (1934) 243